Hydro-acoustic and tsunami waves generated by the 2012 Haida Gwaii earthquake: Modeling and in situ measurements

Ali Abdolali[1,2], Claudia Cecioni[2], Giorgio Bellotti[2], and James T. Kirby[1]

[1]Department of Civil and Environmental Engineering, Center for Applied Coastal Research, University of Delaware, Newark, Delaware, USA, [2]Department of Engineering, Roma Tre University, Rome, Italy

Abstract Detection of low-frequency hydro-acoustic waves as precursor components of destructive tsunamis can enhance the promptness and the accuracy of Tsunami Early Warning Systems (TEWS). We reconstruct the hydro-acoustic wave field generated by the 2012 Haida Gwaii tsunamigenic earthquake using a 2-D horizontal numerical model based on the integration over the depth of the compressible fluid wave equation and considering a mild sloped rigid seabed. Spectral analysis of the wave field obtained at different water depths and distances from the source revealed the frequency range of low-frequency elastic oscillations of sea water. The resulting 2-D numerical model gave us the opportunity to study the hydro-acoustic wave propagation in a large-scale domain with available computers and to support the idea of deep-sea observatory and data interpretation. The model provides satisfactory results, compared with in situ measurements, in the reproduction of the long-gravitational waves. Differences between numerical results and field data are probably due to the lack of exact knowledge of sea bottom motion and to the rigid seabed approximation, indicating the need for further study of poro-elastic bottom effects.

1. Introduction

Submarine earthquakes can generate long-gravitational waves (tsunamis), that propagate at the free surface, and pressure waves (hydro-acoustic waves), which oscillate between the seabed and the free surface due to the compressibility of sea water. Tsunami waves can travel for long distances and are known for their dramatic effects on coastal areas. Hydro-acoustic waves travel much faster than the tsunami itself, i.e., at the speed of sound in water; their presence in a pressure record therefore can anticipate the arrival of the tsunami. Several investigations have been carried out [*Nosov*, 1999; *Stiassnie*, 2010; *Chierici et al.*, 2010; *Cecioni et al.*, 2014a; *Abdolali et al.*, 2014] to study the physical characteristics of hydro-acoustic waves, clarifying that there exists a relationship between these pressure waves and their tsunamigenic source. Low-frequency hydro-acoustic waves generated by seabed motion have been measured during the Tokachi-Oki 2003 tsunami event [*Nosov et al.*, 2007], by the JAMSTEC (Japan Agency for Marine-earth Sciences and TEChnology) observatory. *Nosov and Kolesov* [2007] and *Bolshakova et al.* [2011] have processed the in situ bottom pressure records in order to estimate amplitude, duration, and velocity of bottom displacement. They also presented the results of a 3-D finite difference numerical model reproducing the generated hydro-acoustic waves, and compared the computed signals with the in-situ observations. More recently, the 28 October 2012 a $M_w = 7.8$ earthquake occurred off the West coast of Haida Gwaii archipelago, Canada. *Cassidy et al.* [2014] defined the event as the first major thrust recorded along the predominantly strike-slip fault plane, which generated a tsunami with a significant run up of over 7 m in several inlets on the archipelago. No significant damage resulted, as the region adjacent to the fault rupture is an uninhabited National Park, and the tsunami was limited to the west coast of the islands where there are no settlements or significant coastal structures. The seismic parameters of this earthquake have been analyzed by *Lay et al.* [2013]; moreover, they solved the nonlinear shallow water equations with a vertical velocity term to account for weakly dispersive waves by means of the finite difference model NEOWAVE [*Yamazaki et al.*, 2009], and successfully compared the results with the tsunami observations.

This paper presents numerical modeling of tsunami and hydro-acoustic waves generated by the 2012 Haida Gwaii earthquake. The earthquake is modeled starting from the USGS data and by using the *Okada* [1985] formula to reconstruct the residual seabed displacement. The wave field is modeled solving depth-integrated mild-slope equation of *Sammarco et al.* [2013] by means of the Finite Element Method. Model
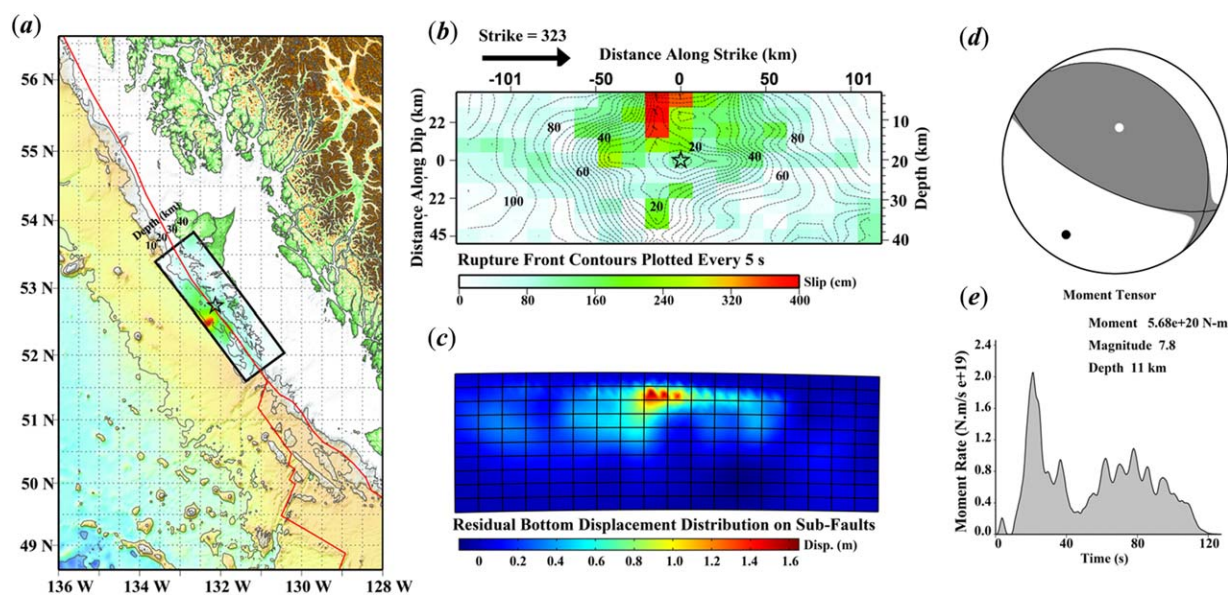
Figure 1. (a) Surface projection of the slip distribution. The red lines indicate major plate boundaries. Black star is the epicenter location. (b) Cross section of slip distribution. The strike direction of the fault plane is indicated by the black arrow. The slip amplitude is shown in color. Contours show the rupture initiation time in seconds. (c) Residual vertical bottom displacement distributed on 180 subfaults. (d) Visual representation of the focal mechanism derived from the estimated moment tensor. (e) Moment rate function describing the rate of moment release with time after earthquake origin. The plots are taken from National Earthquake Information Center (NEIC) of United States Geological Survey (USGS) at http://comcat.cr. usgs.gov/earthquakes/eventpage/pde20121028030408820_14\#scientific_finite-fault.

results are compared with field data recorded, during the 2012 Haida Gwaii event, by the Deep-ocean Assessment and Reporting of Tsunamis (DART®) network (http://nctr.pmel.noaa.gov/queenchar-lotte20121027/) and by the Ocean Network Canada at NEPTUNE observatories (http://www.oceannetworks. ca/haida-gwaii-earthquake-and-tsunami). The paper is structured as follows: section 2 describes the 2012 Haida Gwaii earthquake and consequent waves and provides information on the instruments that recorded the event, whose data are then interpreted and used to compare the results of the numerical model. Section 3 describes the model to simulate the tsunami event in compressible fluid. In section 4, discussions and conclusions are given.

2. 2012 Haida Gwaii Earthquake: Analysis of In Situ Observations

At 28 October 2012, 03:04 UTC, a powerful $M_w = 7.8$ earthquake struck central Moresby Island in the Haida Gwaii archipelago, Canada (Figure 1). The earthquake hypocenter was located (52.788°N, 132.101°W) at a depth of 14 km. This was the largest earthquake to hit Canada since 1949, when an 8.1 magnitude quake hit west of the Haida Gwaii Islands (epicenter at 53.62°N, 133.27°W). The 2012 earthquake occurred as an oblique-thrust faulting on the boundary between the Pacific and North America plates. The Pacific plate actually moves approximately north-northwest with respect to the North America plate at a rate of about 50 mm/yr. The National Earthquake Information Center (NEIC) reports a strike of 323° and dip of 25° for this earthquake event.

Figure 1 shows the main seismic parameters of the event. Figure 1a presents the surface projection of the slip distribution as determined by *Lay et al.* [2013]. The slip distribution on the fault plane is shown in Figure 1b. Contours show the rupture initiation time in seconds with average rupture speed of $V_r = 2.3$ km/s (the rupture time ranges between 0.8 and 74.4 s). Figure 1c shows the residual vertical bottom displacement, calculated by the Okada formula [*Okada*, 1985]. The bottom displacement took place in time intervals ranging from 2.4 to 10 s. The rupture surface is approximately 130 km along the strike direction and 40 km along the dip, and has been divided in 180 subfault elements whose dimensions are 14 and 10 km in the strike and dip directions, respectively. In Figure 1d, the moment tensor for nodal planes is shown. Shaded areas show quadrants of the focal sphere in which the *P* wave first-motions are away from the source, and unshaded areas show quadrants in which the *P* wave first-motions are toward the source. The dots

ABDOLALI ET AL.   959
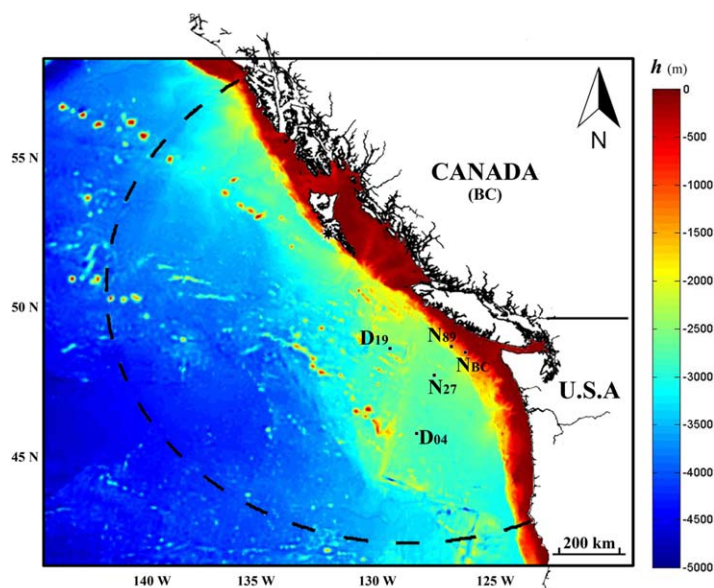
Figure 2. Bathymetry data of the west Canadian and USA coast (ETOPO1 data). The epicenter position is marked with a black star. The black-dashed line delimits, together with the coastline, the domain of the numerical computations.

represent the axis of maximum compressional strain (in black, called the "*P*-axis") and the axis of maximum extensional strain (in white, namely the "*T*-axis") resulting from the earthquake. Figure 1e describes the moment release rate in time after earthquake origin. All the mentioned seismic data are provided by the Advanced National Seismic System (ANSS) Comprehensive Catalog of the U.S. Geological Survey (USGS), available at web site reported in Figure 1.

Free surface and bottom pressure data have been collected during this earthquake by the DART network and by Ocean Network Canada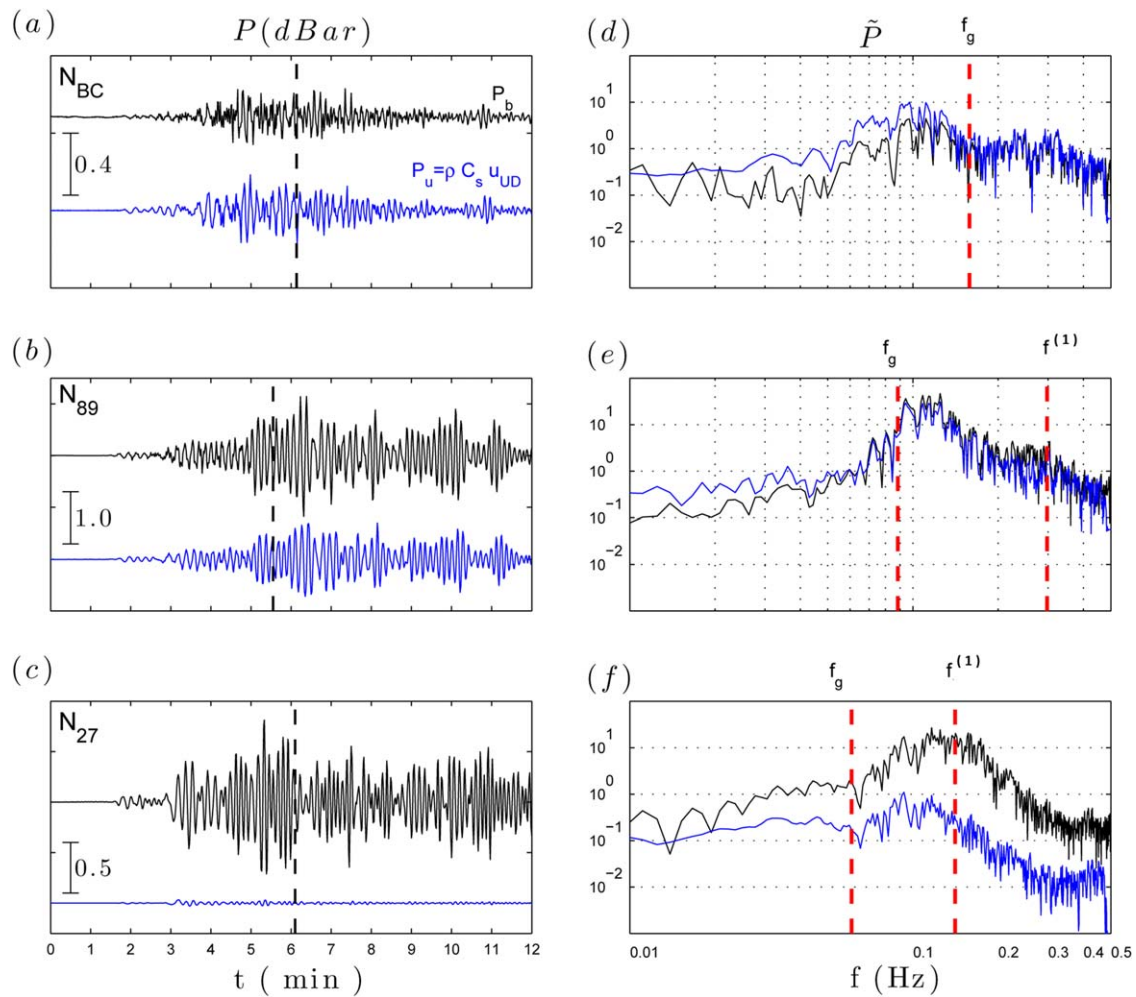. Both networks have instruments located approximately 600 km south the earthquake epicenter. Location of observatories which recorded the waves generated by the 2012 earthquake are shown in Figure 2, together with bathymetric information and the open-sea boundary of the numerical domain (dashed line) described below. The DART network has been deployed by the National Oceanic and Atmospheric Administration (NOAA), to support real-time forecasting of tsunami events. The closest DART instruments that recorded the 2012 earthquake event are: DART46419 (48°45'59"N 129°37'57"W) at 2775 m water depth and 480 km south of the epicenter, and DART46404 (45°51'18"N 128°46'30"W) at 2793 m water depth, 810 km south of the epicenter. Hereinafter, the name of these two stations will shortened, respectively, as D_{19} and D_{04}. Tsunami warning was issued after recording strong signatures, which began at 3:04 UTC, for a large stretch of the North and Central coast of the Haida Gwaii region and eastward to Hawaii. Later the tsunami alarm was limited, canceled, or downgraded. Ocean Network Canada operates cabled observatories from 100 to 2600 m seaward of southwest coast of Vancouver Island in the northeast Pacific. In this paper, we consider data recorded by three submarine observatories: CORK ODP1027 located 640 km south of epicenter at Cascadia Basin (47°45.7560'N 127°45.5527'W) in 2660 m water depth (hereinafter, N_{27}); Bullseye BPR 889, 590 km south of epicenter, at Clayoquot Slope (48°40.2501'N 126°50.8779'W) in 1258 m water depth (N_{89}); Barkley Canyon (Upper Slope) 640 km far from epicenter close to the coast (48°25.6379'N 126°10.4851'W), in 392 m water depth (N_{BC}). These observatories are equipped with many instruments, including bottom pressure records and seismometers. In the hydro-acoustic wave frequency band, as introduced later, the bottom pressure component P_u generated by local ground motion can be obtained from the vertical component (up-down) of bottom velocity (u_{UD}), according to Joukowsi Formula [*Landau and Lifshitz*, 1987]

$$P_u = u_{UD} \rho c_s, \tag{1}$$

where ρ and c_s are, respectively, the water density and the sound celerity in water, here assumed to be constant with values $\rho = 1030$ kg/m^3 and $c_s = 1480$ m/s. Note that the horizontal components of the sea bottom velocity (u_{EW} and u_{NS}) have a minor influence on the wave form and subsequently are excluded from further analysis. Pressure signals recorded by the bottom pressure records of the Ocean Network Canada P_b are shown in Figure 3 as black lines. Figures 3a, 3b, and 3c refer to the data at N_{BC}, N_{89}, and N_{27}, respectively. We have added in all the plots the pressure data P_u (blue lines), calculated using equation (1) from the on-site seismometer data. On the right-side plots, the corresponding spectra are plotted. In order to interpret the spectra, let us define the characteristic frequencies for gravitational and hydro-acoustic waves. The characteristic gravitational wave frequency is $f_g = \sqrt{g/h}$, where h is the water depth and $g = 9.81$ m/s^2 is the

Figure 3. Bottom pressure records (black lines) measured at the three stations of Ocean Network Canada (N_{BC}, N_{89}, and N_{27} from (a) top to (c) bottom) and the corresponding spectrum from (d) to (f), the pressure perturbation (blue lines) obtained by the vertical component of the seabed velocity during earthquake (equation (1)). The black vertical-dashed lines represent the computed arrival time at each stations from the earthquake epicenter of the hydro-acoustic signal traveling at c_s velocity. The red vertical-dashed lines represent the characteristic gravitational wave frequency f_g and first hydro-acoustic mode $f^{(1)}$.

gravitational acceleration. Additional resonators in compressible water column are characterized by a set of natural frequencies:

$$f^{(n)} = \frac{(2n-1)c_s}{4h}, \tag{2}$$

where $n = 1, 2, \ldots$ is the index of the hydro-acoustic mode. The f_g is always smaller than the minimal natural frequency $f^{(1)}$. Therefore, three frequency bands are determined: "Gravitational waves" ($f < f_g$), "Forced oscillations" ($f_g < f < f^{(1)}$), and "Hydro-acoustic waves" ($f > f^{(1)}$). Bottom oscillations within "Gravitational waves" and "Forced oscillations" bands generate gravitational waves. "Forced oscillations" and "Hydro-acoustic waves" bands are responsible for generation of hydro-acoustic waves [*Matsumoto et al.*, 2012]. The characteristic frequencies for each location are indicated by dashed vertical red lines in Figure 3. At N_{BC} shallow water node (392 m deep), the spectra of P_b and P_u show a good agreement within "Forced oscillations" range, although the 1 Hz bottom pressure gauge cannot capture the first 0.96 Hz hydro-acoustic mode. For N_{89} station ($f^{(1)} = 0.31$ Hz), the P_b and P_u spectra are almost coincident for "Forced oscillations" ($f_g < f < f^{(1)}$) and "Hydro-acoustic waves" ($f > f^{(1)}$). For "Gravitational waves" band, the P_b and P_u spectra turn out to be different. It can be seen from Figure 3 that for the case of both N_{BC} and N_{89} stations, the time series plotted in Figures 3a and 3b are generated locally within "Forced oscillations"
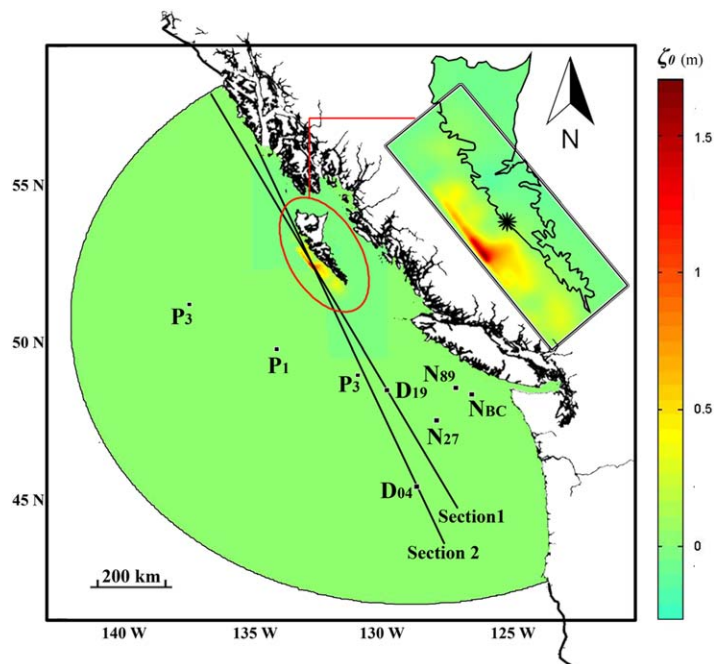
Figure 4. Vertical residual seabed displacement on the numerical domain. The points N_{27}, N_{89}, and N_{BC} represent the Ocean Network Canada observatories location, the points D_{19} and D_{04} represent the DART buoys locations and the points P_1, P_2, and P_2 represent the selected point in front of activated fault in deep sea.

and "Hydro-acoustic waves" bands (Figures 3d and 3e). In other words, the pressure records are not contaminated by remote sources. The reason behind this fact is the "depth effect" introduced later in section 3.1. These stations indeed are located very close to the fault boundary, and therefore ground shaking would be expected in that area. On the other hand, at N_{27} observatory (Figure 3c), the bottom pressure perturbation is mainly generated in the remote areas including proposed subfault for 2012 Haida Gwaii earthquake shown in Figure 1. Moreover, station N_{27} is located in deeper water (2660 m), where the hydro-acoustic waves propagate
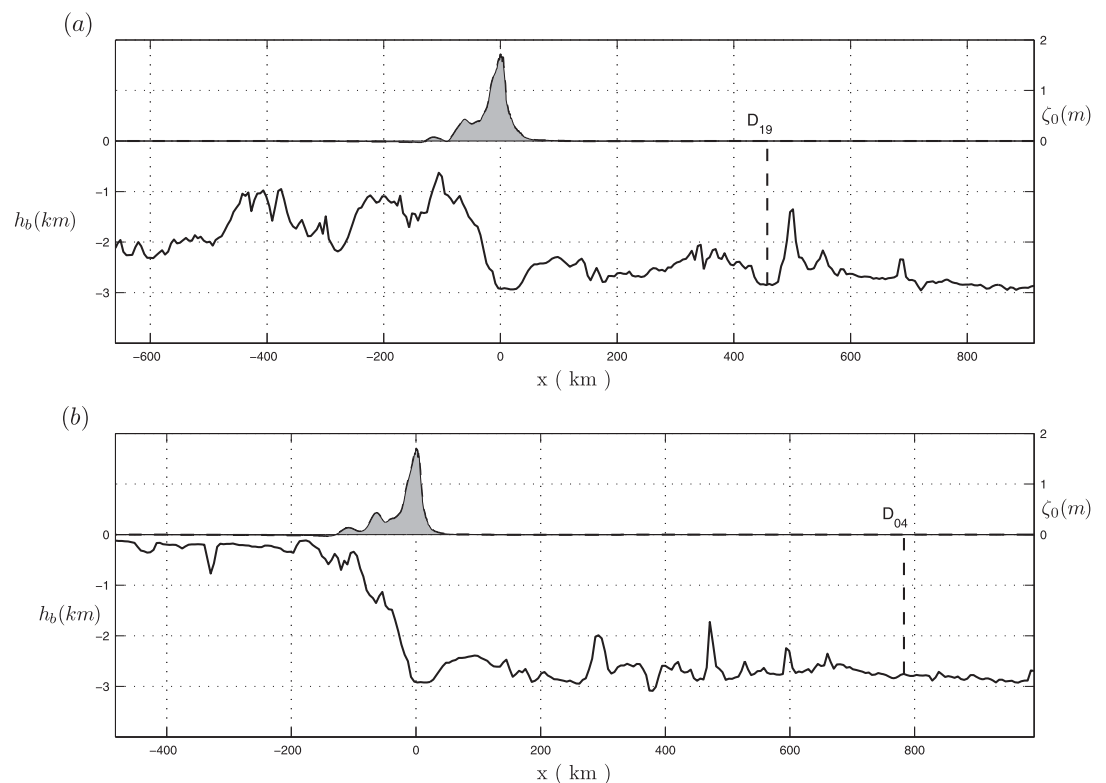
Figure 5. Residual seabed displacement (ζ_0) and water depth (h_b) for the two vertical sections of Figure 4, which cross the 2012 Haida Gwaii earthquake epicenter with each of the two DART stations. As it can be noted that the earthquake's horizontal extension for these sections is about 200 km.
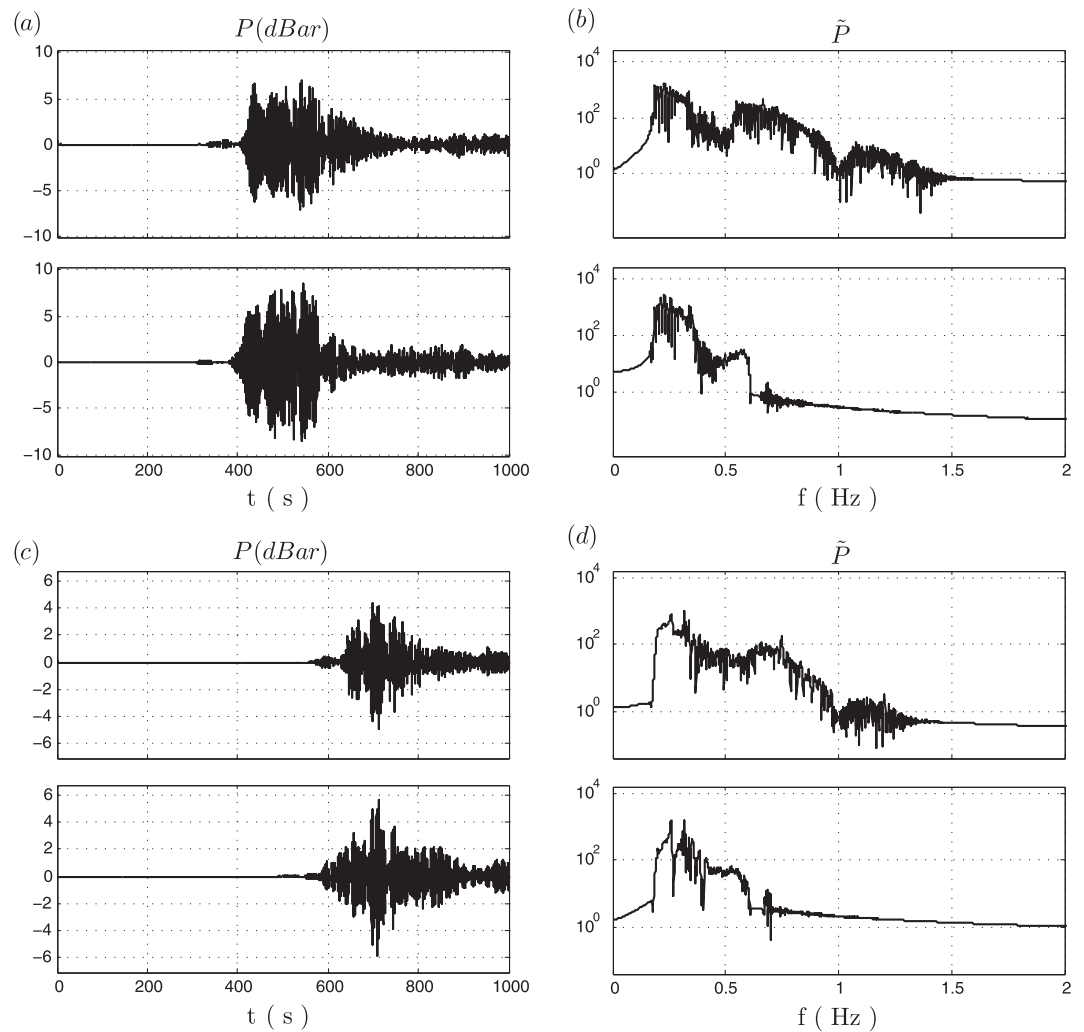
Figure 6. (left) Pressure time series and (right) their frequency spectra at (a, b) D_{19} and at (c, d) D_{04}. Comparison between the solution of the 3-D reference model (top) and the solution of the depth-integrated equation (bottom).

without depth frequency filtering effects [*Cecioni et al.*, 2014b]. The tiny bottom motion at N_{27} position in contrast to N_{BC} and N_{89} stations proves that bottom pressure records at N_{27} are not generated locally. We note that the first signature of hydro-acoustic waves arrives sooner than the hydro-acoustic travel time from the epicenter, possibly indicating the contribution of faster propagating seismic waves within the solid Earth [*Maeda and Furumura*, 2013; *Maeda et al.*, 2013; *Kozdon and Dunham*, 2014].

3. Numerical Simulations

The wave generation and propagation in weakly compressible (first-order approximation of fluid density and pressure), inviscid and irrotational fluid is expressed in terms of the fluid velocity potential $\Phi(x, y, z, t)$, within the framework of linearized wave theory:

$$\begin{cases} \Phi_{tt} - c_s^2 \nabla^2 \Phi - c_s^2 \Phi_{zz} = 0 \\ \Phi_{tt} + g\Phi_z = 0 & \text{at} \quad z = 0 \\ \Phi_z + \nabla h \cdot \nabla \Phi + h_t = 0 & \text{at} \quad z = -h(x, y, t) \end{cases}, \tag{3}$$

where ∇ and ∇^2 are, respectively, the gradient and the Laplacian in the horizontal plane x, y, while subscripts denote partial derivatives.
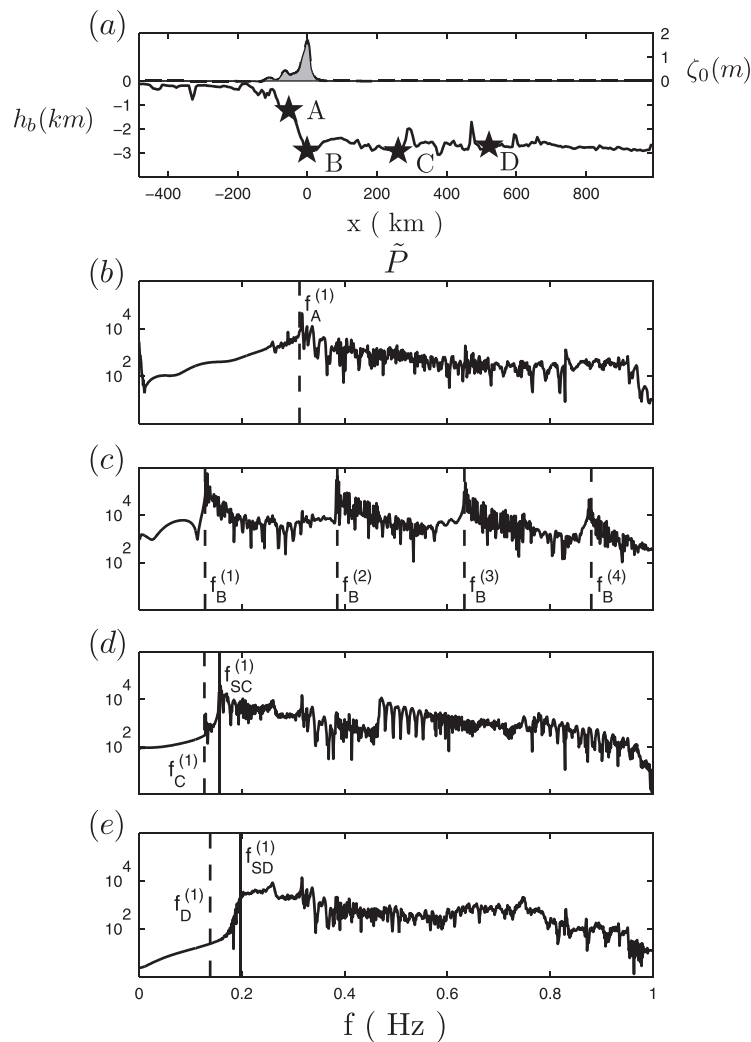
Figure 7. Sea bed pressure spectra computed solving the 3-D wave equation. The plots (b) to (e), respectively, refer to points A ($h = 1220$ m), B ($h = 2916$ m), C ($h = 2945$ m), and D ($h = 2705$ m) along the section reported in the top plot (a). The dashed lines indicate the natural acoustic frequencies corresponding to observation depth while the solid lines represent the first acoustic mode for the minimum water depth between generation area and observation point.

The wave generation is modeled at the bottom boundary, $z = -h(x, y, t)$, where $h(x, y, t) = h_b(x, y) - \zeta(x, y, t)$, and ζ expresses the bottom displacement given by the earthquake. The solution of problem 3 is given by an infinite sum of natural modes, Φ

$$(x, y, z, t) = \sum_{n=0}^{\infty} \phi_n(x, y, z, t)$$
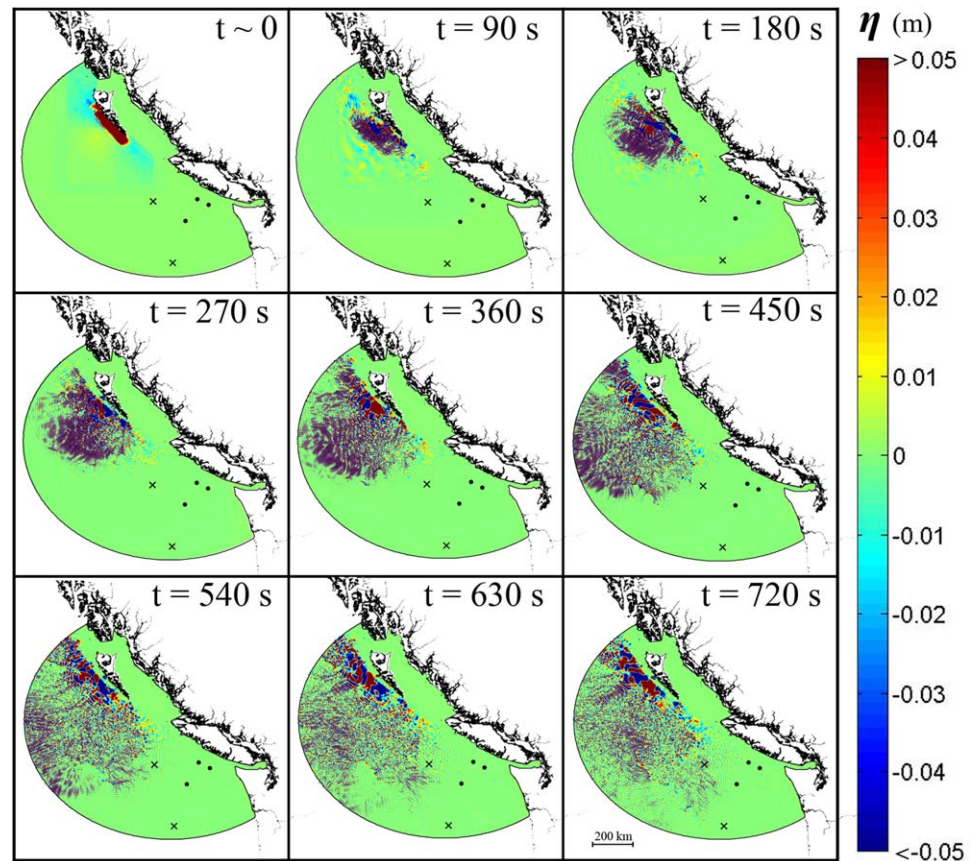$$= \sum_{n=0}^{\infty} \psi_n(x, y, t) f_n(z), \text{ and can}$$

be obtained by means of separation of variable, considering for each mode ψ_n and f_n. The solution of the later function are the classic eigenfunctions of the constant depth homogeneous problem, which is valid for the mildly sloped seabed:

$$f_n(z) = \frac{cosh[\beta_n(h_b + z)]}{cosh(\beta_n h_b)}, \quad (4)$$

where β_n's are the roots of the dispersion relation

$$\omega^2 = g\beta_n \tanh(\beta_n h_b). \quad (5)$$

For the first mode ($n = 0$), β_0 is real and is the mode associated with the gravity surface wave, i.e., the tsunami; for the other modes ($n \geq 1$), namely the hydro-acoustic modes, β_n is purely imaginary and they are responsible for acoustic oscillations of the water body. *Sammarco et al.* [2013] via a proper application of the averaging technique to problem (3), in the hypothesis of constant c_s and mild sloped seabed ($\nabla h \ll kh$), found a depth-integrated equation whose hyperbolic form is:

$$\psi_{n_{tt}}\left(\frac{C_n}{c_s^2} + \frac{1}{g}\right) - \nabla \cdot (C_n \nabla \psi_n) + \left(\frac{\omega^2}{g} - \beta_n^2 C_n\right)\psi_n = h_t D_n. \quad (6)$$

Equation (6) was named mild-slope equation in weakly compressible fluid (MSEWC). Superposition of the solutions, ψ_n, of equation (6) for each mode leads to complete modeling of the fluid potential generated by a fast seabed motion.

In equation (6), the terms $C_n(x, y)$ and $D_n(x, y)$ are given by

$$C_n(x, y) = \int_{-h_b}^{0} f_n^2 dz = \frac{2\beta_n h_b + \sinh(2\beta_n h_b)}{4\beta_n \cosh^2(\beta_n h_b)}, \quad (7)$$

Figure 8. Snapshots of the free surface (η) hydro-acoustic perturbation given by the 2012 Haida Gwaii earthquake. The three points identify the positions of the three Neptune stations, while the two crosses the positions of the DART stations. $t = 0$ refers to the time of occurrence of the earthquake.

$$D_n(x,y) = \frac{1}{\cosh^2(\beta_n h_b)} \frac{\int_{-h_b}^{0} f_n \, dz}{\int_{-h_b}^{0} f_n^2 \, dz} = \frac{4\tanh(\beta_n h_b)}{(2\beta_n h_b + \sinh(2\beta_n h_b))}. \tag{8}$$

For incompressible fluid, i.e., in the limit $c_s \to \infty$, the MSEWC reduces to the mild-slope equation (MSE) for surface gravity waves [*Berkhoff*, 1972] extended to allow for bottom motion [*Cecioni and Bellotti*, 2010a, 2010b]. A detailed derivation of equation (6) can be found in *Sammarco et al.* [2013]. In the time domain, the MSEWC reproduces the fluid potential characteristic of a narrow frequency band wave spectrum, centered around the value of a carrier frequency ω, which determines the variables β_n, C_n, and D_n. A simulation of a broad spectrum thus requires that the problem be divided into a set of narrow frequency bands, and then equation (6) is solved for each band and the results are superimposed. Hereinafter, in the following two subsections are discussed the solutions of equation (6) to reproduce the gravity wave ($n = 0$) and the hydro-acoustic wave ($n \geq 1$). In both cases, a set of many equation as (6), one for each specific frequency, are solved. The results are presented separately because tsunami and hydro-acoustic wave energy occurs at different and not coincident frequency bands.

The 2012 earthquake event at Haida Gwaii archipelago, Canada, has been reproduced numerically solving the MSEWC, equation (6). The model domain is reported in Figure 2; it covers an area of about $1.55 \cdot 10^6$ km^2 of the Pacific Ocean, bounded by the Canadian and USA coasts and by the dashed black line in the open ocean. Figure 2 shows the bathymetric data used in the numerical simulations, taken from the National Geophysical Data Center (NGDC) database ETOPO1 (http://www.ngdc.noaa.gov/mgg/global/global.html). The seabed motion, reconstructed using Okada formula, is mainly an uplift movement, with a
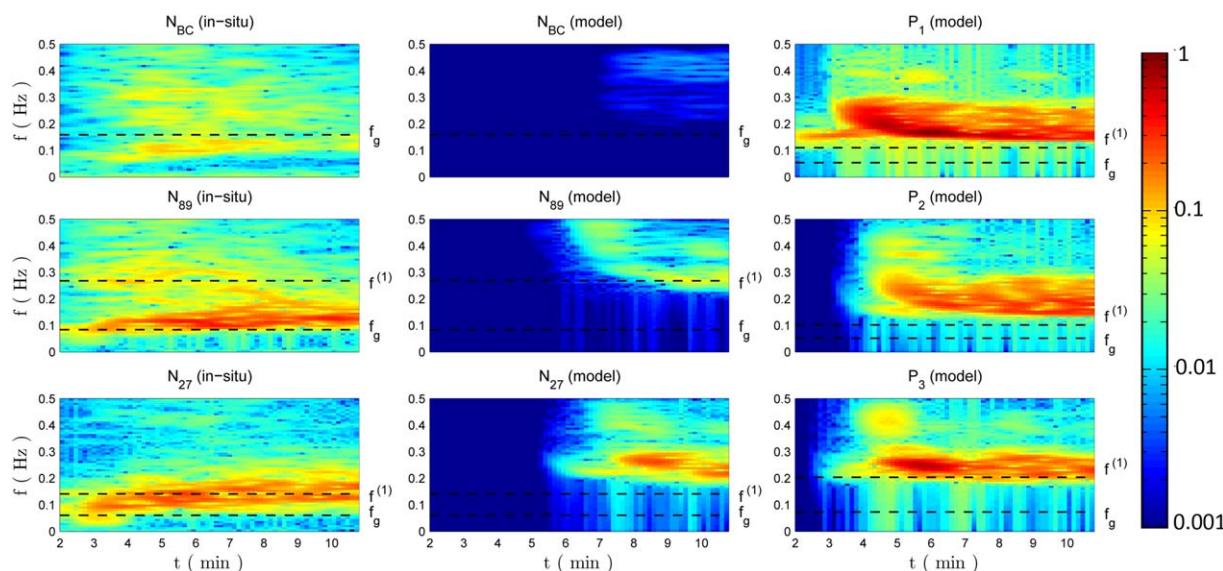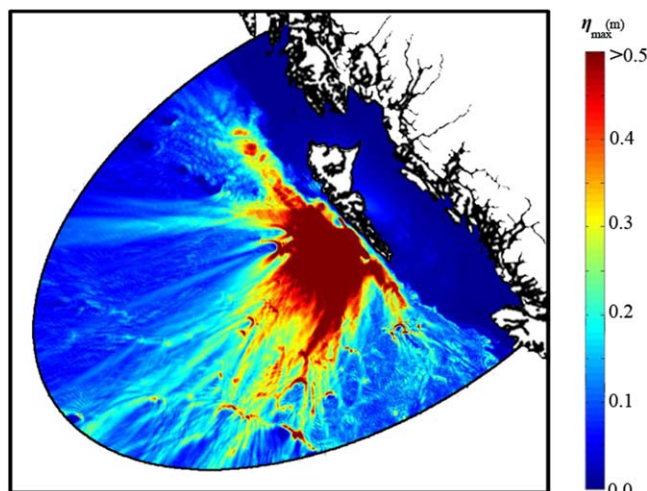
Figure 9. Spectrograms of the bottom pressure normalized by dividing by maximum value. The first column refer to the in situ bottom pressure recorded at N_{BC}, N_{89}, and N_{27}; the second and third columns of plots refer to the simulated hydro-acoustic bottom pressure at the Neptune stations and at points P_1, P_2, and P_3 depicted in Figure 4.

maximum value of $\zeta_0 = 1.6$ m. Unlike the traditional incompressible tsunami models, which often use the residual vertical displacement of the bottom as the initial free surface displacement, in this depth-integrated wave model, the transient time-spatial sea bottom motion is considered for both tsunami and hydro-acoustic modes. The vertical bottom velocity is assumed to be [*Nosov and Kolesov*, 2007]:

$$\zeta_t = \frac{\zeta_0}{2}\left[1 - \cos\left(\frac{2\pi(t-t_0)}{\tau}\right)\right][H(t-t_0) - H(t-t_0-\tau)],\qquad(9)$$

where $H(t)$ is the Heaviside step function and τ is the duration of the bottom displacement. Spreading of the rupture front, starting from epicenter to the far edge of earthquake zone, has been reproduced with a velocity of $V_r = 2.3$ km/s. In the model, the duration of the seabed displacement is assumed everywhere constant equal to $\tau = 6.28$ s. t_0 is the initial time of seabed deformation, which for each point distant r from the epicenter, is obtained as $t_0 = r/V_r$.

3.1. Hydro-Acoustic Wave Model

The modeling of hydro-acoustic waves has been carried out by solving the MSEWC (6) for $n \geq 1$ and for a number of frequencies within a finite range. The simulation of a full 3-D model in the whole area of interest is unreasonably computationally expensive, therefore validation of MSEWC has been carried out by comparison with the solution of the complete 3-D problem expressed by equation (3), along vertical cross sections of the computational domain. The orientation of these two sections is shown in Figure 4 and chosen as the line

Figure 10. Maximum absolute values of the free surface (η) of the hydro-acoustic wave generated by the Haida Gwaii earthquake on 28 October 2012.
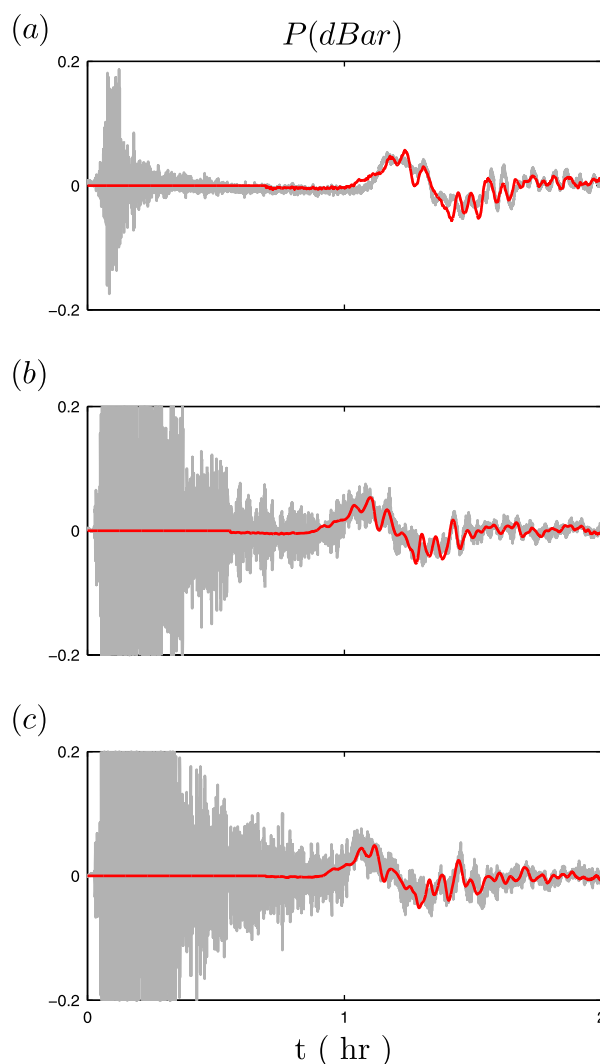
Figure 11. Pressure time series as measured by the NEPTUNE observatories (gray lines) and as calculated by the model for gravity wave (red lines). Plots (a), (b), and (c) correspond to N_{BC}, N_{89}, and N_{27}, respectively. $t = 0$ refers to the time of occurrence of the earthquake.

intersecting the earthquake epicenter and each of the two DART stations. Figure 5 shows the water depth, h_b, and the residual seabed dislocation, ζ_0, along the two cross sections. The comparison of the two models has been done for different points along both cross sections, presenting an overall good agreement. Figure 6 shows the comparison at the position of the two DART stations. Figures 6a and 6b refer to the results at D_{19} in section 1, while Figures 6c and 6d refer to the results at D_{04} in section 2.

In Figure 6, the pressure signals at the sea-bottom both in time (Figures 6a and 6c) and frequency (Figures 6b and 6d) domains are shown. In each plot, the top plot presents the solution of the 3-D problem, while the bottom plot presents the MSEWC solution. The two models provide similar results in the time domain, where arrival time and propagation features of the hydro-acoustic modes show good agreement, even if just the first hydro-acoustic mode has been reproduced and the limited frequency range $f = 0.1$–0.8 Hz has been solved using the MSEWC. These comparisons validate the depth-integrated equation for real bathymetry and enable us to optimize the model. It has been further verified that the reproduction of frequencies outside of the range $f = 0.1$–0.8 Hz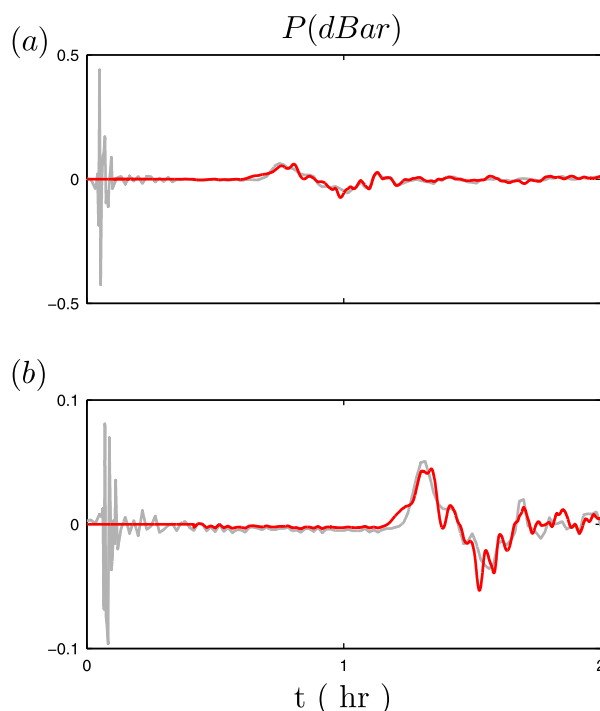, and relative to second and higher hydro-acoustic modes, increases the computational costs without providing a substantial improvement of the results accuracy.

In order to investigate how the variable bathymetry affects the hydro-acoustic wave propagation, four positions along the vertical section 2 have been selected (see Figure 7a): points A and B are located on the earthquake zone at 1200 and 2900 m water depth; points C and D are 250 and 500 km far from epicenter at 2950 and 2700 m water depth, respectively. Figure 7 presents the frequency spectra of the numerically reproduced bottom pressure perturbations for these four positions: plots b, c, d, and e, respectively, for the positions A, B, C, and D.

Hydro-acoustic waves oscillate at the resonating frequency, given for each mode by equation (2), which is therefore inversely proportional to the water depth where these waves are generated. This resonating frequency $f^{(n)}$, namely cutoff frequency [*Tolstoy*; 1963], identifies at each water depth the lower limit of frequencies associated with propagating modes, whereas $f < f^{(n)}$ are characteristic of evanescent modes. In the case of section 2, where the source area covers the shallowest and deepest depths along the section, the minimum frequency for the first mode is 0.13 Hz for the depth of 2950 m. Traveling into shallower water or over sea mounts, the shallower depths do not let the frequencies lower than $f^{(n)}$ to propagate. Figure 7b

Figure 12. Pressure time series as measured at DART buoys (gray lines) and as calculated by the model for gravity wave (red lines). The plots (a) and (b) correspond to D_{19} and D_{04} stations, respectively. $t = 0$ refers to the time of occurrence of the earthquake.

shows with the vertical dashed line the cutoff frequency of the first mode at the local water depth ($f_A^{(1)} = 0.31$ Hz) and it is distinguishable that the pressure signal is filtered for frequencies lower than $f_A^{(1)}$. Figure 7c presents the pressure spectrum at the observation point located on the maximum seabed dislocation at 2900 m water depth; here the spectrum presents higher peaks on the first four acoustic modes $f_B^{(1)} = 0.13$, $f_B^{(2)} = 0.38$, $f_B^{(3)} = 0.64$, and $f_B^{(4)} = 0.88$ Hz (dashed lines). Propagating away from the source zone, the spectrum can be enriched and filtered by higher frequencies representing shallower water normal modes. To reach point C, only frequencies higher than 0.16 Hz cross the shallower area. The solid line in Figure 7d represents the first acoustic mode for the minimum water depth between generation area and point C with 2400 m water depth ($f_{SC}^{(1)} = 0.16$ Hz). Although the first acoustic mode corresponding to local water 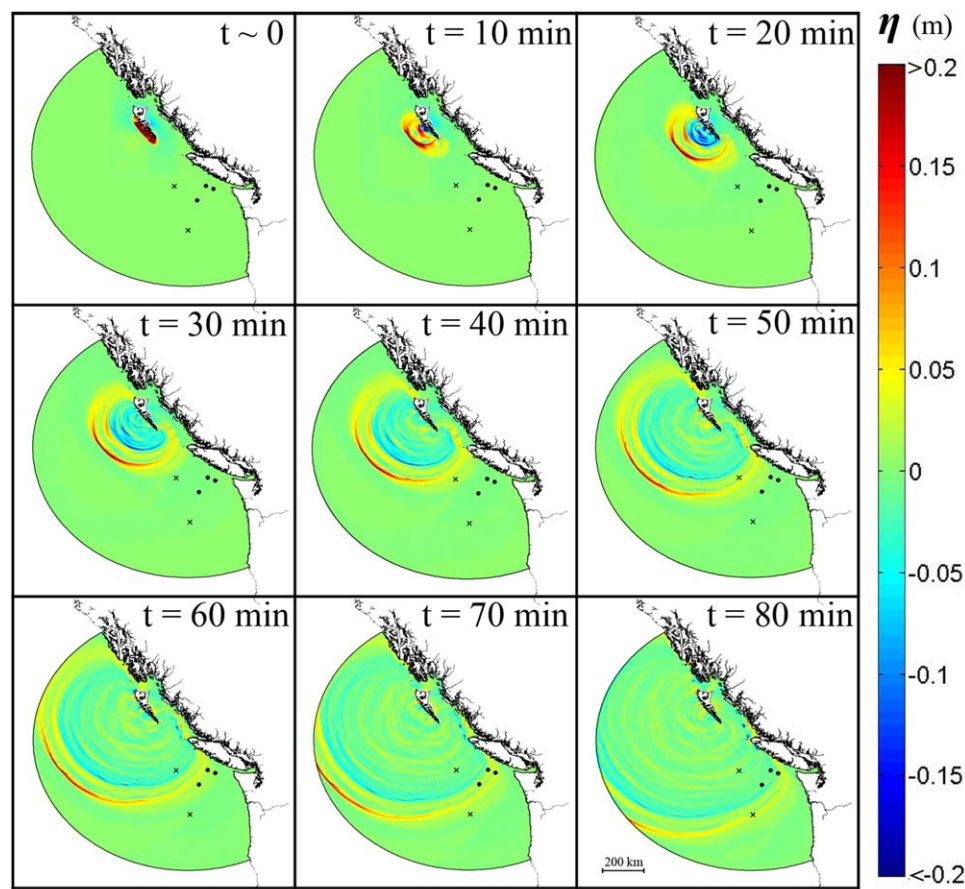depth of point C ($f_C^{(1)} = 0.12$ Hz), shown by dashed line, allows waves with lower frequencies to pass, the spectrum is previously filtered by the shallower area. Figure 7e emphasizes that a higher barrier before point D with 1900 m water depth has barricaded propagation of pressure waves with frequencies lower than 0.2 Hz ($f_{SD}^{(1)}$).

In order to correctly reproduce the hydro-acoustic wave field by means of Finite Element Method in the domain of Figure 2, a maximum element mesh size of 1 km has been chosen, for a total number of 3,000,000 triangular elements. Solutions were obtained using a high-speed computer equipped with 12 cores i7 3.20 GHz CPU and 64 GB RAM. The computational time for solving 720 s with a time step of 0.05 s was about 600 h. The results of this large-scale simulation are shown in Figure 8 in term of free surface elevation, $\eta(x, y, t)$. It can be seen that a complicated perturbation is formed at the free surface and propagates at the sound celerity in water over the entire domain in 12 min after the event. The wave field shows that the hydro-acoustic waves do not propagate upslope; maximum values of hydro-acoustic wave amplitude are in deeper water close to the generation area.

Spectrograms of bottom pressure are presented in Figure 9 for three Ocean Neptune Canada observatories and three selected points in front of active fault at different water depths, as shown in Figure 4. Each spectrogram is normalized by dividing the maximum value among all six points in order to show the ratio of wave amplitudes at different distances and depths. The local characteristic gravitational wave frequency f_g and first acoustic mode $f^{(1)}$ are shown in horizontal lines. The arrival time of low-frequency hydro-acoustic signals, traveling with sound celerity in water from the nearest part of the assumed fault is correctly estimated by the model. Regarding the frequency range of bottom pressure records, we have divided extraction points into three categories: (1) deeper than source area, (2) shallower than source area, and (3) within source area depth. The points P_1 and P_2 fall into category 1 are at 3400 and 3700 m water depths. Therefore, it is expected that points P_1 and P_2 capture all the frequency range generated at the source. At category 2 N_{BC} and N_{89} observatories, where the cutoff frequency is higher than the first acoustic mode at source area ($f^{(1)} = 0.31$ Hz), the majority of waves cannot reach the observatory stations. In other words, at stations located in a shallow depth like N_{BC}, the model calculates tiny pressure wave with large frequencies. It shows that the spectrum has been filtered while ascending the slope. Similarly, at N_{89} station, the pressure waves with frequencies lower than $f^{(1)} = 0.3$ Hz at water depth of 1258 m, has not reached the observatory.

Figure 13. Snapshots of the free surface (η) gravity wave perturbation given by the 2012 Haida Gwaii earthquake. The three points identify the positions of the three Neptune stations, while the two crosses the positions of the DART stations. $t = 0$ refers to the time of occurrence of the earthquake.

Point P_3 (category 3) is located at 1850 m depth, hence, it can capture the wave frequencies higher than 0.2 Hz. Although the point N_{27} is deep enough to capture wave frequencies larger than 0.14 Hz, it is surrounded by shallower areas and the majority of waves have been filtered before reaching point N_{27}. The results of numerical simulation are shown in Figure 10, in terms of maximum absolute water level. Here the propagation path of hydro-acoustic waves toward deep sea orthogonal to fault plane can be interpreted as waves propagate farther, their energy spreads and their intensity decreases. The scattered sea-mounts restrict passage of the lower frequencies.

3.2. Tsunami Waves

Numerical simulation of the long–gravitational waves generated by the 2012 Haida Gwaii earthquake has been performed by solving the zero mode of MSEWC (equation (6)). As for the hydro-acoustic modes equation (6) is solved by means of Finite Element Method on the numerical domain, which has been discretized in triangular elements with a maximum size of 2.5 km. The computational time is 12 h (on the same computer described in section 3.1) for simulation of 2 h real time. The frequencies in the range $f = 0$–0.03 Hz, with a $df = 0.002$ Hz, have been solved to reconstruct the gravitational wave field. Results of the zero mode simulation are presented in Figures 11 and 12, in terms of bottom pressure time series at the Ocean Network Canada observatories and at the DART buoys, respectively. In both figures, the red lines show the results of the numerical model, while the gray lines represent the pressure signals recorded at the instruments. The model simulates the tsunami wave magnitude and arrival time properly compared with observation. In Figure 11, the plots a, b, and c refer, respectively, to the observatories N_{BC}, N_{89}, and N_{27}. The comparison between the model and the field data at the Neptune Canada observatories is in good agreement in terms of amplitude, period, and arrival time of the pressure signal given by the long gravity wave transit. The field pressure

data, however, include the pressure variation given by the ground motion and the precursor waves. Figure 12 shows the comparison results at the DART station D_{19}, plot a, and D_{04}, plot b. Both numerical and field data reveal that tsunami waves arrived at point D_{19} and D_{04}, respectively, 35 and 70 min after the event. Although the sampling frequency of DART records is not sufficient to resolve the fast elastic oscillation and low-frequency hydro-acoustic waves (0.066 Hz), there is some perturbation few minutes after the earthquake. The bottom displacement has not occurred at the mentioned points, keeping in mind that DART stations are far from epicenter and not located on the subduction zone. Even neglecting the missing peaks due to low sampling frequency of DART buoys, the low-frequency wave peaks in the available time series are larger than the following tsunami waves (0.5 and 0.1 dBar correspond to D_{19} and D_{04}). Figure 13 depicts the time history of generation and propagation of tsunami waves in the computational domain. The plot shows that the residual bottom dislocation is almost transferred to the sea surface. The wave front starts spreading and covers the entire domain after 2 h. Comparison between Figures 8 and 13 shows that, except during the first stages of the generation process, the significant difference between the speed of low-frequency and tsunami waves leads to the different location of hydro-acoustic and tsunami waves fronts in time.

4. Conclusions

Reproduction of long-gravitational waves spreading proportional to square root of the water depth, and low-frequency hydro-acoustic waves traveling with the sound celerity in water, have been studied for 2012 Haida Gwaii earthquake in the framework of linear potential theory, using a hyperbolic mild-slope equation for weakly compressible fluids (MSEWC) [*Sammarco et al.*, 2013]. Here we show a first application of MSEWC to numerically reproduce wave generation and propagation in weakly compressible fluid in a large-scale domain, overcoming the computational difficulties of three-dimensional models. The numerical model is validated against a fully 3-D linear model for the case of varying water depth. The comparison has been done in order to understand the physics of low-frequency propagation in the far-field in order to utilize deep-sea observatories for enhancement of TEWS. At present, the 2-D numerical model is not able to reproduce the intensity of hydro-acoustic wave field. However, it shows the importance of deep-sea observatories where the depth effect does not affect the arriving wave spectrum. It is worth citing that due to the lack of knowledge about spatiotemporal bottom motion in numerical modeling the calculation for hydro-acoustic waves is still a rough estimate of the exact result. In other words, we have assumed sea bottom deformation spreads uniformly from epicenter ($V_r = 2.3$ km/s) taken place with mean bottom displacement duration ($\tau = 6.23$ s) in a certain rectangular fault. Therefore, the aftershocks and tiny bottom motions along the active fault orientation, responsible for local elastic waves, are neglected. In addition, the role of bottom elasticity of porous sedimentary layer in decay of hydro-acoustic waves [*Chierici et al.*, 2010] is neglected. The underlying sedimentary layer causes a shift of dominant spectral peaks toward lower values [*Abdolali et al.*, 2015]. This behavior depends on sediment thickness and density. More importantly, damping of hydro-acoustic waves due to diffraction at sea bottom and through porous medium is caused by high bulk viscosity of sediment. The bulk viscosity of sediment causes a shift of spectral peaks to lower frequency values as well as damping. For very large bulk viscosity, the result for rigid and porous bottom is the same [*Chierici et al.*, 2010; *Abdolali et al.*, 2015]. On the other hand, comparison of long-gravitational wave records from Ocean Network Canada observatory and DART buoys with numerical results shows that assumption of rigid bottom without sedimentary layers is reasonable for long-gravitational wave. Analysis of bottom pressure records shows the role of sea bottom topography on the generation of normal acoustic modes. While the pressure waves spread out, the sea mounts and shallower areas filter the spectrum. This fact demonstrates the necessity of deep-sea observatory for proper hydro-acoustic detection. The present study points out practical suggestions for deep-sea observatory deployment near potential tsunamigenic zones. The availability of seismograms recorded at the observatories allows the interpretation of signals in order to distinguish the local generated elastic waves. The complete modeling of these waves could, in principle, dramatically improve the effectiveness of a TEWS [*Chierici et al.*, 2010], given the recent advances in deep-sea measurement technology.

References

Abdolali, A., C. Cecioni, G. Bellotti, and P. Sammarco (2014), A depth-integrated equation for large scale modeling of tsunami in weakly compressible fluid. *Coastal Engineering Proceedings*, *1*(34), A.S.C.E., currents 9., 1–13, Seoul, Korea, doi:10.9753/icce.v34.currents.9.

Abdolali, A., J. T. Kirby, and G. Bellotti (2015), Depth-integrated equation for hydro-acoustic waves with bottom damping. *J. Fluid Mech.*, *766*, doi:10.1017/jfm.2015.37.

Berkhoff, J. C. W. (1972), Computation of Combined Refraction - Diffraction. Coastal Engineering Proceedings, *1*(13), pp. 471–490, A.S.C.E., vancouver, doi:10.9753/icce.v13.%p.

Bolshakova, A., S. Inoue, S. Kolesov, H. Matsumoto, M. Nosov, and T. Ohmachi (2011), Hydroacoustic effects in the 2003 Tokachi-oki tsunami source, *Russ. J. Earth Sci.*, *12*, 1–14, ES2005, doi:10.2205/2011ES000509.

Cassidy, J. F., G. C. Rogers, and R. D. Hyndman (2014), An overview of the 28 October 2012 Mw 7.7 Earthquake in Haida Gwaii, Canada: A tsunamigenic thrust event along a predominantly strike-slip margin, *Pure Appl. Geophys.*, *171*(12), pp. 3457–3465, doi:10.1007/s00024-014-0775-1.

Cecioni, C., and G. Bellotti (2010a), Modeling tsunamis generated by submerged landslides using depth integrated equations, *Appl. Ocean Res.*, *32*(3), 343–350.

Cecioni, C., and G. Bellotti (2010b), Inclusion of landslide tsunamis generation into a depth integrated wave model, *Nat. Hazards Earth Syst. Sci.*, *10*(11), 2259–2268.

Cecioni, C., G. Bellotti, A. Romano, A. Abdolali, P. Sammarco, and L. Franco (2014a), tsunami early warning system based on real-time measurements of hydro-acoustic waves, *Proc. Eng.*, *70*(C), 311–320.

Cecioni, C., A. Abdolali, G. Bellotti, and P. Sammarco (2014b), Large-scale numerical modeling of hydro-acoustic waves generated by tsunamigenic earthquakes, *Nat. Hazards Earth Syst. Sci. Discuss.*, *2*(7), 4629–4658, doi:10.5194/nhessd-2-4629-2014.

Chierici, F., L. Pignagnoli, and D. Embriaco (2010), Modeling of the hydroacoustic signal and tsunami wave generated by seafloor motion including a porous seabed, *J. Geophys. Res.*, *115*, C03015, doi:10.1029/2009JC005522.

Kozdon, J. E., and E. M. Dunham (2014), Constraining shallow slip and tsunami excitation in megathrust ruptures using seismic and ocean acoustic waves recorded on ocean-bottom sensor networks, *Earth Planet. Sci. Lett.*, *396*, 56–65.

Landau, L. D., and E. M. Lifshitz (1987), *Fluid Mechanics, V. 6 of Course of Theoretical Physics*, 2nd English ed. revised, Elsevier.

Lay, T., L. Ye, H. Kanamori, Y. Yamazaki, K. F. Cheung, K. Kwong, and K. Koper (2013), The October 28, 2012 Mw 7.8 Haida Gwaii underthrusting earthquake and tsunami: Slip partitioning along the Queen Charlotte Fault transpressional plate boundary, *Earth Planet. Sci. Lett.*, *370*, 57–70, doi:10.1016/j.epsl.2013.05.005.

Maeda, T., and T. Furumura (2013), FDM simulation of seismic waves, ocean acoustic waves, and tsunamis based on tsunami-coupled equations of motion, *Pure Appl. Geophys.*, *170*(1–2), 109–127.

Maeda, T., T. Furumura, S. Noguchi, S. Takemura, S. I. Sakai, M. Shinohara, and S. J. Lee (2013), Seismic and tsunami wave propagation of the 2011 off the Pacific Coast of Tohoku earthquake as inferred from the tsunami coupled finite difference simulation, *Bull. Seismol. Soc. Am.*, *103*(2B), 1456–1472.

Matsumoto, H., S. Inoue, and T. Ohmachi (2012), Some features of water pressure change during the 2011 Tohoku earthquake, in *Proceedings of the International Symposium on Engineering Lessons Learned from the 2011 Great East Japan Earthquake*, Japan Association for Earthquake Engineering (JAEE), Tokyo, Japan.

Nosov, M. A. (1999), Tsunami generation in compressible ocean, *Phys. Chem. Earth, Part B*, *24*(5), 437–441.

Nosov, M. A., and S. V. Kolesov (2007), Elastic oscillations of water column in the 2003 Tokachi-Oki tsunami source: In-situ measurements and 3-D numerical modelling, *Nat. Hazards Earth Syst. Sci.*, *7*(2), 243–249.

Nosov, M. A., S. V. Kolesov, A. V. Denisova, A. B. Alekseev, and B. V. Levin (2007), On the near-bottom pressure variations in the region of the 2003 Tokachi-Oki tsunami source, *Oceanology*, *47*(1), 26–32, doi:10.1134/S0001437007010055.

Okada, Y. (1985), Surface deformation due to shear and tensile faults in a half-space, *Bull. Seismol. Soc. Am.*, *75*(4), 1135–1154.

Sammarco, P., C. Cecioni, G. Bellotti, and A. Abdolali (2013), Depth-integrated equation for large-scale modelling of low-frequency hydroacoustic waves, *J. Fluid Mech.*, *722*, R6.

Stiassnie, M. (2010), Tsunamis and acoustic-gravity waves from underwater earthquakes, *J. Eng. Math.*, *67*(1), 23–32, doi:10.1007/s10665-009-9323-x.

Tolstoy, I. (1963), The theory of waves in stratified fluids including the effects of gravity and rotation, *Rev. Mod. Phys.*, *35*(1), 207.

Yamazaki, Y., Z. Kowalik, and K. F. Cheung (2009), Depth integrated, non hydrostatic model for wave breaking and run up, *Int. J. Numer. Methods Fluids*, *61*(5), 473–497.